PbS colloidal quantum dot solar cells: ink-based scalable fabrication

Laura de la Fuente Esteban

July 10, 2022

BSc. thesis
in Physics

PbS colloidal quantum dot solar cells: ink-based scalable fabrication

Laura de la Fuente Esteban

15 ECTS thesis submitted in partial fulfilment of a
BSc. degree in Physics

Supervisors
Prof. dr. M.A. Loi
H. Wang

Examiners
Prof. dr. M.A. Loi
Prof. dr. P. Rudolf

PbS colloidal quantum dot solar cells: ink-based scalable fabrication
(PbS CQDSC: ink-based scalable fabrication)

15 ECTS thesis submitted in partial fulfilment of a BSc. degree in Physics

Faculty of Science and Engineering
Photophysics and OptoElectronics Group
Zernike Institute for Advanced Materials
University of Groningen
Nijenborgh 4
9747 AG, Groningen, The Netherlands

Telephone: +31(0)50 363 8750

Groningen, The Netherlands, July 10, 2022

A mamá, por creer en mí.
Sin ti no sé dónde estaría hoy.

Abstract

The industrial-oriented mounting of cost-efficient solar cells with solution-processable methods, such as blade coating, has been investigated in the presented research. PbS colloidal quantum dots in the form of ink have been used to explore the characterisation and improvement of the reference p-i-n structure. Furthermore, SeMet and L-cysteine have been evaluated to substitute the MPA compound utilised for the p-type layer and to avoid the water dependence of the ligand. The introduction of alternative experimental methods and materials with respect to previous devices shows an outstanding power conversion efficiency (PCE) of 9.42% and a considerable enhancement of the short-circuit current density (JSC).

Contents

Contents

Acknowledgements

In the first place, I would like to thank Maria for giving me the opportunity to become part of her research group to do my thesis and get such valuable experience. This time has felt like the perfect end to my bachelor.

I also want to thank Han for guiding me through this new world of gloveboxes, quantum dots and lab machinery and making me enjoy it.

To all the members of the PO-E group, thank you for being so welcoming and kind from the very first day I arrived.

Finally, I want to thank all the women of my family who have sacrificed their dreams so that later generations of girls could be here, doing what I am doing. I will be forever proud of being the first undergraduate woman in the family. I hope this feels as yours as mine.

En primer lugar, me gustaría agradecer a Maria por haberme dado la oportunidad de formar parte de su grupo de investigación para hacer mi tesis y obtener una experiencia tan valiosa. Este tiempo se ha sentido como el perfecto punto y final a mi carrera.

También quiero dar las gracias a Han por guiarme por este nuevo mundo de cajas de guantes, puntos cuánticos y maquinaria de laboratorio y hacer que lo disfrute.

A todos los miembros del grupo PO-E, gracias por recibirme con los brazos abiertos desde el primer día que llegué.

Finalmente quiero dar las gracias a todas las mujeres de mi familia que han sacrificado sus sueños para que generaciones futuras de niñas puedan estar aquí, haciendo lo que estoy haciendo. Estaré eternamente orgullosa de ser la primera universitaria de la familia. Espero que esto se sienta tan vuestro como mio.

Glossary

AA ammonium acetate

BA butylamine

conc concentration

CQDSC colloidal quantum dot solar cell

DMF N,N-Dimethylformamide

DMSO dimethyl sulfoxide

EDT 1,2-ethanedithiol

EQE external quantum efficiency

ETL electron transporting layer

FF fill factor

HCl hydrochloric acid

HOMO highest occupied molecular orbital

IPA isopropanol

IR infrared

ITO indium tin oxide

JSC short-circuit current density

LUMO lowest unoccupied molecular orbital

MPA 3-Mercaptopropionic acid

Glossary

MPP maximum power point

OA oleic acid

PbS lead sulfide

PCE power conversion efficiency

PTFE polytetrafluoroethylene

PV photovoltaic

QD quantum dot

SeMet selenomethionine

VOC open-circuit voltage

ZnO zinc oxide

1. Introduction

Energy is not destroyed nor created but transformed. Although it can sound poetic, the first thermodynamics law sets the base of almost all physical phenomena. The French physicist Edmond Becquerel put this statement into practice and discovered in 1839 (*1*) how electricity could be produced from solar radiation: it was the beginning of photovoltaics. Since this seminal discovery, the solar cells field has rapidly matured while reaching impressive achievements and responding to the increasing global energy demand the world is currently facing.

Nonetheless, in a society where capitalism and science coexist, not only the most efficient developments succeed but also the cheaper ones. This is why the so-called third-generation solar cells present promising possibilities with respect to their efficiency and costs. This generation aims to use established deposition techniques while working with abundant, non-toxic materials to overcome the limiting efficiencies that conventional solar cells have previously encountered. The objective is to increase the areal costs as the cost per Watt peak decreases, obtaining cheaper and more efficient solar cells (*2*). Third-generation solar cells include organic and dye-sensitized cells, perovskites and quantum dots. The latter has experienced fast growth in the last few decades as they permit great tunability of their electrical and optical properties (*3*). The versatility of their characteristics and nano-size puts them in the field spotlight and presents an optimistic future for colloidal quantum dot solar cells (CQDSCs).

Although they are positioned as the future of solar energy, these emerging technologies have not yet reached the prevailing market. Some difficulties include stability issues, costly fabrication methods or toxicity risks (*3*) (*4*). Developments regarding passivation techniques, device architecture optimization or hot carrier utilization are needed (*5*) in order to make quantum dots available for commercial applications.

Therefore, and as a means to contribute to the pioneering manufacturing techniques focused on commercialization stages, an ink-based lead sulfide (PbS) CQDSC has been reproduced with the purpose of reaching or overcoming the reference values for power conversion efficiency (PCE), open-circuit voltage (VOC), short-circuit current density (JSC) and fill factor (FF) while modifying materials, procedures and methods during the mounting of the device. At the same time, new materials have been tested to substitute the thiol-based 3-Mercaptopropionic acid (MPA) molecule

1

1. Introduction

and offer a novel and water-free approach for the p-doped ink to achieve a superior and complete solution-processable solar cell.

2. Background

2.1. Principles of solar cells

A solar cell is a device capable of converting incoming light into power. Its core structure is based on a semi-conductive material that permits the separation and transport of light-generated excitons and top and bottom electric contacts that enable the collection of higher energy electrons into an external circuit. Solar cells can also include antireflective layers or encapsulants to avoid losses and protect the cell from its environment. Their power resides in the capacity to collect solar energy via the photovoltaic effect due to the semiconductor material's specific atomic structure and energetic configuration.

2.1.1. Conduction

The process in which thermal energy is transferred due to the collision or movement of atoms is called conduction (*6*). In semiconductors, this phenomenon occurs due to the presence of covalent bonds. When the electron gains thermal energy, it delocalises from the covalent bond and liberates from its equilibrium state, reaching a high energy level. In opposition, when the electron is bound to its *original* configuration, it is at a low energy state (i.e. the semiconductor behaves as an insulator). Therefore, the only existence of the covalent bond between two atoms introduces the previously mentioned energy levels. The electron will be found either at the high or the low energy state, never at an immediate level (*7*). The lower energy state is called the **valence band** (E_v), and the energy state at which the electron is free is called the **conduction band** (E_c). In organic semiconductors, the terms lowest unoccupied molecular orbital (LUMO) and highest occupied molecular orbital (HOMO) are better used due to the existence of trap states and a high density of defects (*8*). The minimum energy needed for the electron to break free from the covalent bond is the **band gap** of the semiconductor and is defined as the difference in energy between the valence and conduction band. When this minimum energy is met, the electron will become excited and *jump* from its bound state into a free state, allowing it to participate in conduction. As the electron leaves the valence band to

move about the semiconductor, a hole is created, leaving space for a neighbouring electron to take in. Therefore, the continuous refilling of holes with neighbouring electrons can also be seen as the movement of positive charges through the lattice structure (*7*). This way, not only the electron participates in the conduction process but also the holes which become carriers.

Thus, conduction can be explained as a process which directly results from the motion of the electrons through the allowed bands. Consequently, the electrical properties of a specific material will be determined by the electronic concentration of electrons and holes found in the allowed bands (*9*). Accordingly, three different types of materials can be distinguished depending on their band gap population: insulators, conductors and semiconductors.

2.1.2. Semiconductors

Semiconductor materials are notably relevant for the operation of solar cells due to their optical and electronic properties. The need for a suitable band gap and absorption of the visible and near infrared (IR) spectra makes semiconductors the perfect choice both for the light-harvesting layer and transport layer, as their non-zero band gap permits the photon-excitation of electrons and selective collection of carriers to avoid recombination (*10*). Insulators, for example, do not allow the thermal excitation of electrons into the conduction band as their band gap is too large. On the other hand, conductors experience an overlap of the valence and conduction bands, making the latter partially occupied and hence having high conductivity (*6*). Nevertheless, these materials do not permit the formation of p-n junctions, becoming inadequate for solar cell purposes.

Semiconductors consist of individual atoms bonded together to form an ordered and periodic structure (*11*). The atoms that form these materials are elements found in group IV of the periodic table or combinations of groups II and VI or groups III and V (*12*). The particularity of semiconductor materials is that the electrons *orbiting* the atom's nucleus are part of a covalent bond so that each pair of atoms share two electrons (*7*). At absolute zero, this structure binds the covalent electrons to a specific configuration of the lattice, limiting their movement and localizing them in a particular region (*7*). Nevertheless, at higher temperatures, electrons can break out from these bonds as they gain thermal energy, becoming *free* to move through the lattice and take part in the conduction process. Because of the breaking of these bonds, the generation of electron-hole pairs is induced as a hole is created, and a neighbouring valence electron fills the free space (*11*). Therefore, the number of bonds created in a semiconductor is inherently related to the concentration of holes (p) and electrons (n). The total broken bonds at a particular temperature per cm^3

is called the **intrinsic carrier concentration**[1] and can be described by

$$n_i^2 = np \tag{2.1}$$

2.1.3. Junction

As previously stated, electrons are bound to the lowest available levels at absolute zero and fill the next free states in order of increasing energy. The higher level to which electrons are capable of filling if the semiconductor is at absolute zero is called the **Fermi level** (*12*). If the semiconductor is in thermal equilibrium, no net flux of particles occurs at different points of the material. This leads to a set distribution of particles -described by the Fermi-Dirac distribution- and an equal Fermi level at all points (*12*). Therefore, the most stable energy distribution of electrons can be defined as

$$f(E, E_f, T) = \frac{1}{\exp(\epsilon - \epsilon_F/k_B T) + 1} \tag{2.2}$$

and present consistency with their statistical potential energy (ϵ_F) and their internal energy described by $k_B T$.

Nevertheless, the electronic properties of conductive materials can be intentionally modified by altering the equilibrium described by Equations 2.1 and 2.2. By introducing an impurity atom or due to the presence of a structural defect, the crystal lattice can be changed (*12*). The bonds that previously formed the perfect structure are replaced due to the introduction of dopants. Consequently, the distribution of energy levels is affected and depending on where these new states are localised, the density of electrons or holes will increase or decrease (*12*). The variance of the density of carriers will directly change the position of the Fermi level as the temperature increases, and thus the bands will shift (*13*). How the mentioned shift will occur will depend on the type of doping introduced in the material: p or n-type. The first includes electron acceptor impurities and shows a higher density of holes, while the latter is known as electron donor doping and presents a higher concentration of free electrons (*14*). When the material is p-doped, the Fermi level will shift towards the valence band where there is a deficit of electrons. Analogously, the Fermi level will shift towards the conduction band if the semiconductor is n-type (*14*).

Carriers are separated by the junction of the solar cell. The junction is an interface layer that exists between two semiconductor materials. This region sets apart carriers so that a voltage is produced via diffusion or drift. The most common junction is formed by a p-type layer and an n-type layer called pn-junction. When these two layers become in contact, the Fermi levels of the materials have to align in order to maintain the Fermi level equalization throughout the crystal (*15*). This

---

[1]Note that Equation 2.1 only holds for intrinsic and doped semiconductors in equilibrium.

phenomenon is referred to as band bending. Band bending is directly caused by the movement of carriers from one doped semiconductor to another. The exchange of carriers between layers induces the appearance of an electric field and the formation of the so-called depletion region (*7*). Nevertheless, in this research, the studied junction has a p-i-n structure. In this specific case, an intrinsic region (i) is found between the two doped layers. The electric field, previously mentioned, extends over the whole intrinsic layer, and the alignment of Fermi levels happens through the i-type material (*16*). The incorporation of this new layer also permits the control of the width of the depletion region, which is directly dependent on a good generation of exciton pairs (*17*). The electron-hole pairs are then selected by the electron and hole transport layers due to the band alignment of the materials, leading to a smaller recombination loss (*18*).

2.2. Solar cell characterisation

The performance of solar cells and photovoltaic (PV) devices is determined using various parameters. Typically these are the PCE, the JSC, the VOC, the FF and the external quantum efficiency (EQE). As a means to understand these figures of merit, it is helpful to observe a representative current density versus voltage graph for a solar cell under illumination (Figure 2.1).
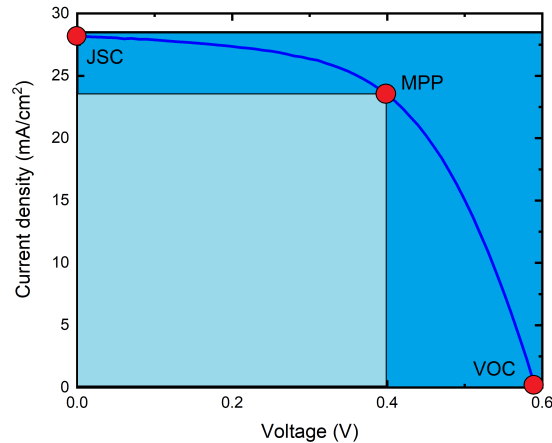

Figure 2.1: **J-V curve**. *J-V graph for an arbitrary solar cell.*

As seen from the J-V graph, JSC refers to the current the cell can extract when there is no voltage bias. Analogously, VOC indicates the circuit's maximum voltage bias that results in a zero current. It corresponds to the light-generated in-built

voltage of the circuit. In other words: when the solar cell experiences illumination, the Fermi level ϵ_F splits into two *quasi*-Fermi levels: ϵ_F^e and ϵ_F^h. The difference between the interchanged energy of electrons and holes due to the splitting of the Fermi level defines the open-circuit voltage (*19*):

$$VOC = q(\epsilon_F^e - \epsilon_F^h) \tag{2.3}$$

being q the electric charge.

The maximum power point (MPP) specifies the point of the curve where the cell's maximum power is generated. It can be defined in relation to the PCE as

$$PCE = \frac{V_{MPP} \cdot J_{MPP}}{P_{in}} \tag{2.4}$$

$$= \frac{MPP}{P_{in}} \tag{2.5}$$

where P_{in} is the incident monochromatic light intensity the cell receives and V_{MPP} and J_{MPP} are the maximum power points for voltage and current, respectively.

The FF is the parameter which determines the ratio of maximum power from a solar cell, and it is defined as

$$FF = \frac{MPP}{VOC \cdot JSC} \tag{2.6}$$

It can also be graphically calculated from the J-V curve by

$$FF = \frac{\text{Area} \ \blacksquare}{\text{Area} \ \blacksquare} \tag{2.7}$$

The more the shape of the J-V curve resembles a square, the higher the FF will be and the more it will approximate, as well, the ideality of a heterojunction as a diode (*12*).

All these parameters are evaluated under a set of variables to ensure globally comparable analyses. The convention is to measure the cell's characterisation at 25°C under 1000 W/m intensity of the standard AM1.5G solar spectrum. This spectrum represents the solar irradiance the Earth receives annually at mid-latitudes after it has been filtered by 1.5 atmospheric volumes (*19*). These conditions are not always available in a laboratory environment; therefore, a solar simulator is used to reproduce these variables. The used experimental devices are further explained in Section 4.3.

Finally, the EQE is the ratio of the number of extracted carriers by the solar cell to the number of photons of the known incident energy. With this parameter, the

cell's spectral response S(λ) under monochromatic light, which indicates the current extracted per incident watt of light (*19*), can be measured. The EQE is calculated by

$$EQE(\lambda) = \frac{hc}{q\lambda} \frac{J(\lambda)}{P_{in}(\lambda)} \tag{2.8}$$

$$= \frac{hc}{q\lambda} S(\lambda) \tag{2.9}$$

where h is Planck's constant, q the elementary charge, c the speed of light and λ the wavelength of the incident light.

2.3. Colloidal quantum dots

2.3.1. Solution-processable PVs

Solution-processable techniques emerged as alternative approaches to fabricating solar cells, allowing the use of methods such as blade and spin coating and presenting new ways of controlling applicable properties. Its manufacturing potential grants it significant competence with the extensively commercialized Silicon solar cells (*19*). Not only their easy processing features make this PV technology compelling, but also their low cost and high efficiency (*20*). Furthermore, materials such as polymers or organic molecules, which are widely used for these techniques, present a high absorption coefficient opening the possibility of the fabrication of nano-size layers (*19*). Nevertheless, solution-processable PV is still a field in research and needs to overcome some obstacles regarding durability and toxicity, among others, in order to reach the commercialization stage (*20*).

2.3.2. PbS quantum dots

Colloidal quantum dots are semiconductor nanocrystals usually formed by an inner inorganic core surrounded by an organic layer of ligands (*21*) that provides stability and solubility in non-polar solvents (*19*). The advantage of colloidal quantum dots is their flexibility regarding the tunability of their electrical and optical properties. Electrical properties can be adjusted depending on the surface ligands used, while optical properties are dependent on the size of the nanoparticles that form the quantum dot (*3*) (*22*). Optical properties arise from the quantum confinement effect (*23*) that these particles experience due to their nano size: carriers in the crystal lattice are confined by the boundary of the quantum dot, and free energy

levels are quantised (*19*). This effect only occurs when the size of the nanoparticles is small enough so that it is comparable to or smaller than the exciton Bohr radius of the material (*24*), which is defined as

$$r_{Bohr} = \frac{\epsilon_r \hbar^2}{e^2} \left(\frac{1}{m_e} + \frac{1}{m_h} \right) \tag{2.10}$$

where ϵ_r indicates the dielectric constant of the material, $\hbar$ the reduced Planck's constant, e the elementary charge, and m_e and m_h the effective masses of the electron and the hole, respectively.

The popularity of lead chalcogenide materials, such as PbS, lies in their exceptional photosensitivity characteristics in the near IR spectrum (*25*). PbS, furthermore, offers an ease synthesis that allows to reproduce monodisperse, defect-free nanocrystals (*19*) and good stability (*26*). Its large exciton Bohr radius ($\sim$ 18 nm) confers it an exceptional position for solar cell applications as it enhances the quantum confinement effect (*26*), leading to a higher multiple exciton generation (*27*), meaning that each photon can activate more than one electron-hole pair (*4*). As such, the band gap of PbS quantum dots can be precisely configured within the existing energy range by modifying its size (*24*).

2.3.3. Ligands

Charge transport in colloidal quantum dots depends on the proximity from one quantum dot to another and only becomes possible if they are close enough so that the wave functions of charge carriers overlap with neighbouring quantum dots (*24*). The coupling energy β can approximately estimate the distance between the quantum dots, as it is directly dependent on the tunnelling rate Γ:

$$\beta = h\Gamma \propto \exp\left(-2\Delta x \sqrt{\frac{2m^*}{\hbar^2} \Delta E} \right) \tag{2.11}$$

being m^* the effective mass of the charge carrier and Δx and ΔE the interdot potential energy barrier in width and height, respectively.

Therefore, and as observed in Equation 2.11, the coupling is significantly dependent on the separation between quantum dots and, consequently, on the length of the surfactant ligands (*19*). As previously discussed, colloidal quantum dots contain a surrounding organic layer of ligands, such as oleic acid (OA), that offers stabilization. Nevertheless, this layer of ligands also appears as a hindering facet as it significantly obstructs charge transport due to their size and can ultimately diminish the device performance (*18*). Therefore, replacement procedures are used before deposition processes to substitute these ligands with shorter-chain organic molecules, such as

thiols, and enhance the transport properties of the nanocrystals (*28*) (*29*). This process is known as **ligand exchange**.

Two different ligand exchange procedures exist: solid-state (layer-by-layer) and solution phase-transfer. The layer-by-layer technique consists of the deposition of various layers. In order to achieve a thin layer deposition, the synthesised quantum dots are dispersed in a non-polar solvent to be stabilised. A few drops of the solution are placed onto the substrate and subsequently spin-coated. Next to it, short-chain ligands, such as MPA or 1,2-ethanedithiol (EDT), are dissolved in a polar solvent and deposited on the film so that the ligand exchange can take place. Finally, the excess ligands are removed by washing them with the previously used solvent. Overall, the fabrication of devices using this type of ligand exchange is not only time-consuming and costly regarding materials but also can have incomplete coverage of ligand as the reaction time and space are limited (*24*).

On the other hand, the phase-transfer method is more oriented toward industrialisation processes as it does not require so many steps and can be reproduced at large scale (*24*). In the first place, colloidal quantum dots are dispersed in a non-polar solution and mixed with a polar solution containing the short-chain organic molecules. After shaking or stirring the mixture, the transfer of phases becomes visibly noticeable: the quantum dots shift to the polar phase, and the non-polar phase turns into a transparent liquid layer. This last layer is removed, and the remaining solution is washed two or three times with the previously used non-polar solvent (typically hexane or octane). After the washing, an antisolvent is added to proceed with the precipitation step (*30*), and the mixture is then centrifuged. After the centrifugation process, the supernatant is removed, and the pellet is dissolved, creating a quantum dot ink ready to use in different fabrication techniques, such as blade and spin-coating or ink-jet printing.

3. Device structure

The original device on which this thesis is based on consists of an indium tin oxide (ITO) anode lying on glass and capped by a PbS-MPA p-type layer, a PbS CQD n-type layer treated with a mixture of lead halogen salts on top, then a zinc oxide (ZnO) electron transporting layer (ETL) that also works as a hole-blocking layer, and a final aluminium back contact (Figure 3.1). The J-V characteristics of the champion cell can be consulted in Table 5.2.
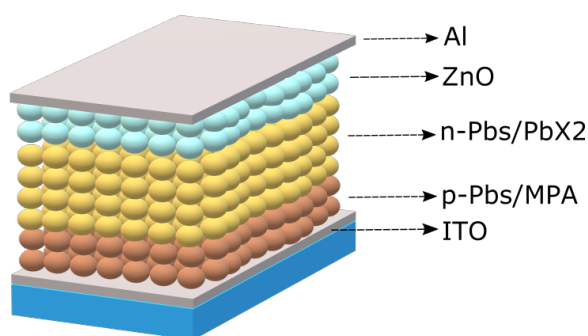

Figure 3.1: **Reference device**. *Structure of the reproduced device during the research.*

The reference device was reproduced as a first attempt to observe its stability and characterisation, changing some procedures during its fabrication. After some trials, the best results were obtained with the following structure: 15x15 ITO anode on glass capped by a PbS-MPA p-type layer, a PbS CQD n-type layer treated with PbX_2/ammonium acetate (AA), a ZnO-isopropanol (IPA) ETL and an aluminium back contact.

As a novel approach, the MPA organosulfur compound used in the p-type ligand exchange was substituted with selenomethionine (SeMet) and L-cysteine. Regardless, the junction's structure is the same at its core. No devices were mounted using these chemicals; only the solubility and the ligand exchange procedures were tested.

4. Experimental methods

4.1. Chemicals

All the used chemicals in this research were purchased from the manufacturer Sigma-Aldrich. Those which were not are specified in their respective section.

4.1.1. PbS

The used PbS nanocrystals were synthesised by the hot injection method with OA ligands by Dr Loredana Protesescu's group in ZIAM.

4.1.2. MPA

The ligand exchange in the p-type layer was executed with MPA. This chemical compound is a bifunctional molecule that contains a thiol group and a carboxylate group.
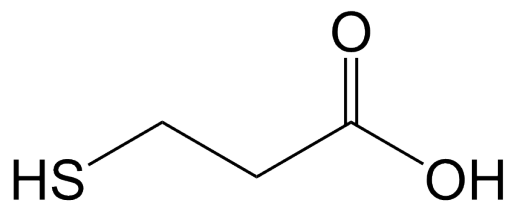

Figure 4.1: **MPA chemical structure**.

4.1.3. PbX$_2$/AA

In order for the ligand exchange to occur for the n-type ink, a mixture of lead halide ligands was used. Following the recipe proposed by Goossens et al. (*31*), a

4. Experimental methods

combination of PbI$_2$, PbBr$_2$ and AA was used. This is referred to as PbX$_2$/AA. The PbI$_2$ and PbBr$_2$ compounds were purchased from TCI.

4.1.4. ZnO

The ETL layer was made using ZnO nanocrystals. These were prepared using zinc acetate dehydrate stirred with methanol and a solution of KOH in methanol. Both solutions were mixed and left for precipitation. The supernatant was removed, and the pellet was washed with MeOH two times. The ZnO nanocrystals were then ready to use and dissolve.

ZnO in IPA

As an alternative approach for the ETL, a ZnO nanoparticle ink in IPA with a concentration of 2.5 wt.%.

4.1.5. SeMet

SeMet was tested for the p-type layer in order to substitute MPA and proceed with the ligand exchange. This amino acid contains a carboxyl, an amino and a selenide group.
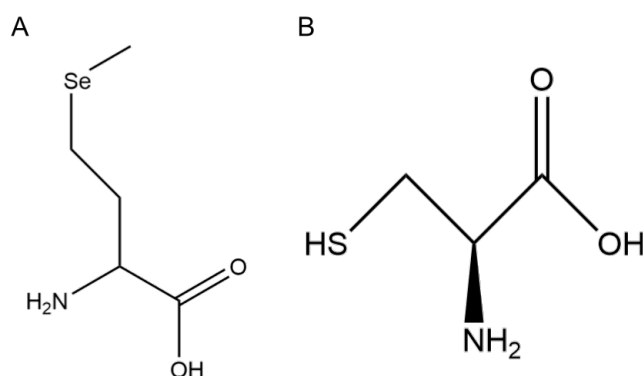

Figure 4.2: **New materials**. SeMet (A) and L-cysteine (B) chemical structures.

14

4.1.6. L-cysteine

L-cysteine in the form of powder was used as an alternative to MPA. It is an amino acid that usually participates in enzymatic reactions and contains a carboxyl, a thiol and an amino group.

4.2. Preparation

4.2.1. p-type ink

In order to prepare this ink, the recipe provided by Goossens et al. (*31*) was followed. It consists of a solution-phase ligand exchange of MPA in N,N-Dimethylformamide (DMF) added to a solution of PbS-OA. The mixture is shaken manually so that the ligand exchange occurs in a few seconds. The next step is washing the solution by removing the hexane in the first place and cleaning it with an equal volume of hexane to remove possible remaining long-chain ligands. Next, the solution is centrifuged at 4500 RCF for 5 minutes so that precipitation occurs. The supernatant is removed, and the pellet is dried and dissolved in a 50:50 solution of butylamine (BA) and water. The ink is filtered with a 0.2 μm polytetrafluoroethylene (PTFE) filter before its usage.

4.2.2. n-type ink

A similar method was executed in order to prepare the n-type ink. PbI_2, $PbBr_2$ and AA powders in DMF are mixed together. The solution is added to PbS-OA in hexane. After that, the mixture is energetically shaken as the ligand exchange occurs. It can be noticed by the colour difference between the two phases, as seen in Figure 4.3. The transparent hexane layer is removed, and next, the polar phase is washed two more times with an equal volume of hexane. After finishing the washing, toluene antisolvent is added to the solution to precipitate the quantum dots (QDs) (*24*). The sample is centrifuged at 4500 RCF for 5 minutes and the supernatant is removed and dried with the help of an N_2 gun. Finally, the supernatant is dissolved with BA and filtered through a 0.2 μm PTFE filter.
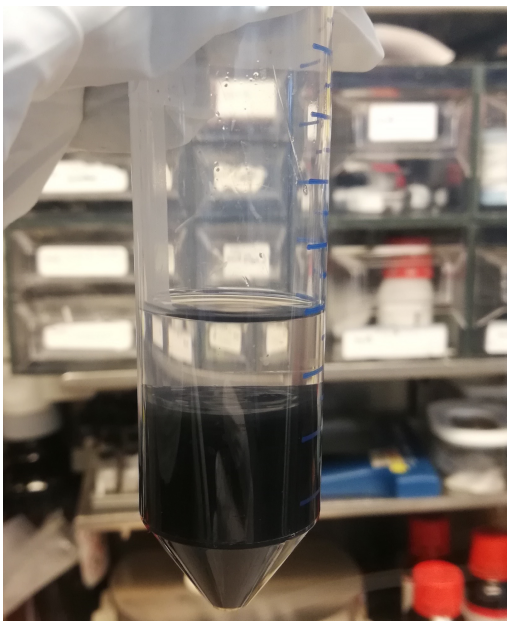
Figure 4.3: **Phase-transfer**. *Ligand exchange between PX_2/AA in DMF and PbS-OA in hexane.*

4.2.3. ZnO layer

The first approach to fabricating the ETL consisted in diluting the priorly prepared ZnO nanocrystals in a 1:1 v/v solution of chloroform and methanol. Nevertheless, ZnO nanocrystals in IPA were used after observing the first results. This chemical is presented in ink, so no previous dissolution is required. The manufacturer indicates to ultrasonicate the ink and filtering it through a 0.45 μm PTFE filter before its usage.

4.3. Device mounting procedures

The fabrication method used for these devices is scalable rather than the usual layer-by-layer technique.

In the first place, the ITO substrates were cleaned with a 10:1 v/v solution of water and extra concentrated soap. Next, following the manufacturer's recommendations, the substrates were sonicated in water, acetone and IPA twice. After completing the cleaning procedure, the ITO substrates were treated with UV ozone for 20 minutes. This ultra-fine treatment permits the enhancement of the substrates' wettability as it removes the surface passivation of organic contaminants (*32*).

As a means to deposit both the p and n-type layers and due to the aqueous nature of the p-type solvent, a blade coater in air was used. This device consists of a heated metal plate with controllable temperature on which a speed-configurable arm lies. A blade is positioned against the arm so that it moves accordingly to the set speed of the machine, and the height at which the blade is from the substrate is adjusted (Table 4.1). The chosen speed for each deposited layer directly affects the pursued thickness: the higher the speed, the thicker the deposited layer. The deposition of the p and n-type layers led to a thickness of 40 and 370 nm, respectively.

Layer	Temperature (°C)	Speed (mm/s)	Height (μm)	Volume (μL)
p-type	70	7.5	200	23
n-type	70	40	200	23

Table 4.1: **Blade coating**. *Parameters used for the deposition of the p and n-type layers.*

After each deposition, the substrates were annealed at 70°C for 30 minutes. All of these steps were conducted in air. This is because, following the p-type deposition, the film must be passivated with O_2. The PbS/MPA layer contains numerous defects and vacancy sites on the QDs surface, which can be avoided if the film is annealed in air as defect passivation using O_2 has been determined to prevent non-radiative recombination and, at the same time, improve the device's performance (*33*), specifically its VOC. Furthermore, if the following post-annealing steps were to be performed in N_2, the former passivation would be lost since the PbS-PbSO$_4$ reaction is reversible at high temperatures (*34*).

The deposition of the ZnO layer was achieved with the aid of a spin coater. With this technique, the deposition of the layer is accomplished via the spinning of the substrate. Some droplets of the ZnO solution are placed on the substrate and then spun so that centrifugal forces spread the fluid, creating the pursued layer. The time, acceleration and speed of the rotatory plate onto which the substrate is placed can be adjusted. The solution of ZnO in chloroform was spin-coated under an N_2 atmosphere due to its evaporation characteristics, while the IPA-based solution was done in air. The speed difference between both solutions (see Table 4.2) was due to the need to control the thickness of the layer to a comparative level. The substrates were then left to anneal for 20 minutes at 70°C. The measured thickness for the ZnO-IPA layer was approximately 36 nm, while the ZnO in chloroform presented a thickness of around 45 nm.

Solution	Speed (rpm)	Acceleration (rpm/s)	Time (s)
Chloroform	3000	1000	30
IPA	2000	1000	30

Table 4.2: **Spin coating**. *Parameters used for the deposition of the ZnO layer.*

4. Experimental methods

The final layer -Al back contact- was assembled using a metal evaporator. The patterned substrates were prepared and placed inside an under-pressured bell at approximately 1.6×10^{-6} mbar, and aluminium rods were evaporated as the deposition of a 100 nm layer was controlled.

Finally, and to obtain the cell's characterisation, the samples were measured in an N_2 atmosphere at a temperature of 295 K regulated with a liquid nitrogen stream. The voltage was modified, and the current was measured with a Keithley 2400 source meter. To simulate the conventional AM1.5 solar spectrum, a Sterunagel Solar constant 1200 metal halide lamp was used, and a Si calibration cell was utilized to place the device under an illumination of 100 mW/cm². The stability testing was also performed with the previous machinery and involved the cell's exposure to a continuous light source during a set period of time. The executed tests consisted of characterisation measurements every 5 minutes for 30 minutes, approximately.

The EQE value was obtained using a monochromatic light created by a 230 W quartz tungsten halogen lamp together with various narrow bandpass filters. The light intensity was quantified with the help of two photodiodes (PD300 and PD300IR), which measured the visible and near IR regions. With respect to the absorbance measurements, these were determined using a Jasco V670 spectrometer.

5. Experimental results and Discussion

5.1. Device

In the first place, the passivation technique was evaluated. ITO substrates on glass were treated in plasma and UV ozone. After the first deposition of the p-type layer, it was noticed that the wettability of the plasma samples was notably worse than the UV-treated ones (Figure 5.1). Plasma treatment led to inhomogeneity of the film and, consequently, to worse performance of the device.
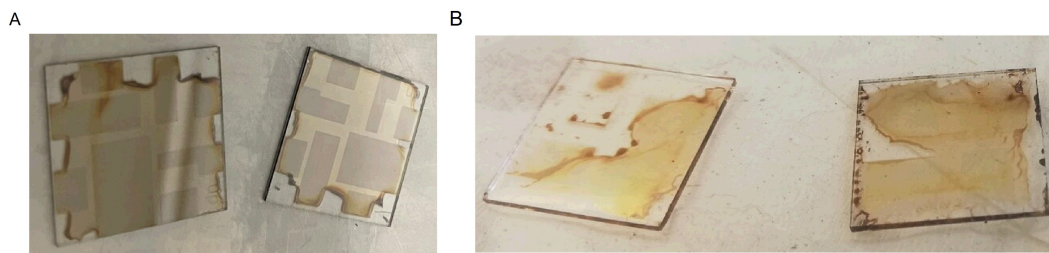

Figure 5.1: ***Passivation treatment comparison****. Films treated in UV-ozone (A) and in plasma (B) capped with the p-type ink.*

The first completed batch consisted of 15x15 mm ITO substrates and comprised two major variables: the received passivation treatment and the ZnO solution used. Although UV-ozone passivation showed better wettability on the films, some substrates were also mounted with no previous treatment. On the other hand, some samples were capped with ZnO dissolved in chloroform, while others used ZnO in IPA.

The best devices, both for chloroform and IPA, were obtained with the UV-treated films. Nevertheless, significant differences in the solar cell performance were observed between the two types of ZnO-capped substrates. The champion device performance

5. Experimental results and Discussion

for each fabricated device and its respective J-V curve can be consulted in Table 5.1 and Figure 5.2.

	Sweep	VOC (V)	JSC (mA/cm^2)	FF	PCE (%)
Champion IPA	Reverse	0.59	28.18	0.57	9.42
Average IPA	Reverse	0.51 ± 0.04	23.57 ± 1.08	0.49 ± 0.03	6.16 ± 0.86
Champion CF	Reverse	0.57	11.57	0.45	2.97

Table 5.1: **Characterisation parameters**. *VOC, JSC, FF and PCE of the champion and average ITO/PbS-MPA/PbS-PbX2/ZnO IPA/Al and ITO/PbS-MPA/PbS-PbX2/ZnO CF/Al devices under one sun illumination.*

IPA samples not only reach a higher PCE but notably enhance the JSC of the films while considerably increasing the other figures of merit. The IPA champion device overcome the reference champion device's PCE, JSC and VOC, although a slightly lower FF is obtained. Overall, the ZnO-IPA statistics show a poorer performance with respect to the champion device. Some problems with the thickness of the n-type layer occurred during the mounting of the second batch of solar cells, which led to a thinner layer (~ 70 nm) and a low posterior JSC, as the intrinsic region of this structure is the primary source of high JSC.

	Sweep	VOC (V)	JSC (mA/cm^2)	FF	PCE (%)
Champion	Reverse	0.57	26.22	0.61	9.04
Average	Reverse	0.54 ± 0.04	24.3 ± 2.1	0.52 ± 0.06	6.8 ± 1.0

Table 5.2: **Reference parameters**. *Characterisation of the champion and average reference devices under one sun illumination.*

Chloroform samples used in Goossens et al. work (*31*) showed impressive figures of merit. Nevertheless, this could not be observed in this research. The wettability of ZnO in chloroform was relatively deficient, and a homogeneous layer through the film could not be obtained. After spin-coating the solution, a radial pattern could be observed (Figure 5.3). This led to a discontinuous and non-uniform layer that directly diminished the charge transport of electrons.

In order to test the stability of the fabricated structure, light soaking tests were performed. The samples were tested on days 2 and 6, and their characterisation was measured. In between measurements, the cells were stored in an N$_2$ atmosphere. Two samples of distinct n-layer thickness were used: sample 10 thinner as blade coated with a speed of 12 m/s and sample 15 thicker -speed 40 m/s. The evolution of all parameters can be consulted in Figure 5.4. It can precisely be observed a considerable light soaking effect that affects the VOC, FF and PCE the most. The short-circuit current experiences a modest increase after 5 minutes of soaking, before it stabilises. This process indicates the presence of a photo-activated process (*31*) due to the passivation that traps in the device undergo. Light soaking effects have also been observed in different QD research (*35*). During the operation of the
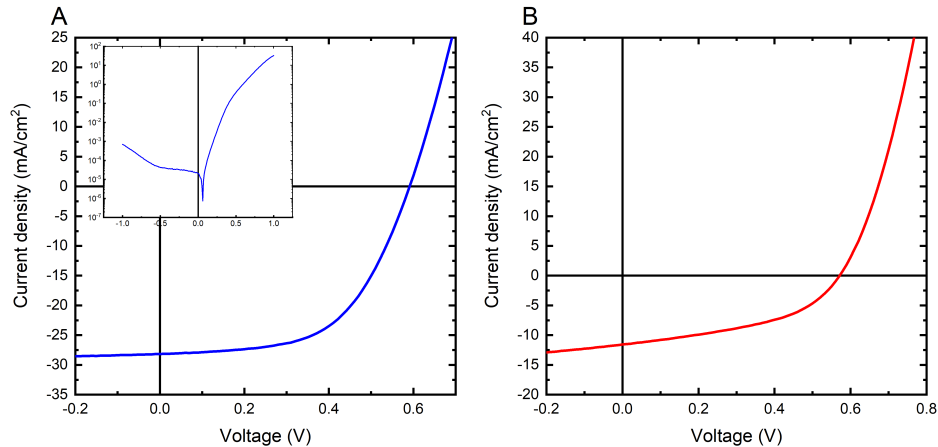
Figure 5.2: **Champion devices**.
(A) The current density versus voltage characteristics of the champion ITO/PbS-MPA/PbS-PbX2AA/ZnO-IPA/Al device right as it was exposed to one sun illumination. The inset shows the absolute current density in the dark right before illumination.
(B) The current density versus voltage characteristics of the champion ITO/PbS-MPA/PbS-PbX2AA/ZnO-CF/Al device right as it was exposed to one sun illumination.
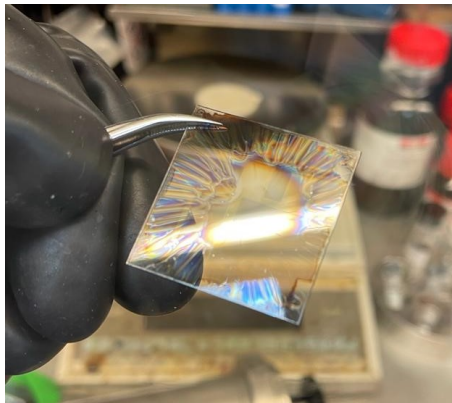

Figure 5.3: **ZnO in chloroform**. Wettability pattern after spin coating the ZnO solution onto the film.

CQDSC, all the parameters increased. Nevertheless, after the devices' storage, the performance of both tested samples worsened as the devices predictably degraded. JSC is the only figure of merit that presents a slight improvement for both devices after six days in an N_2 atmosphere . This could have happened due to a bad calibration or a fluctuation in the regulating temperature.
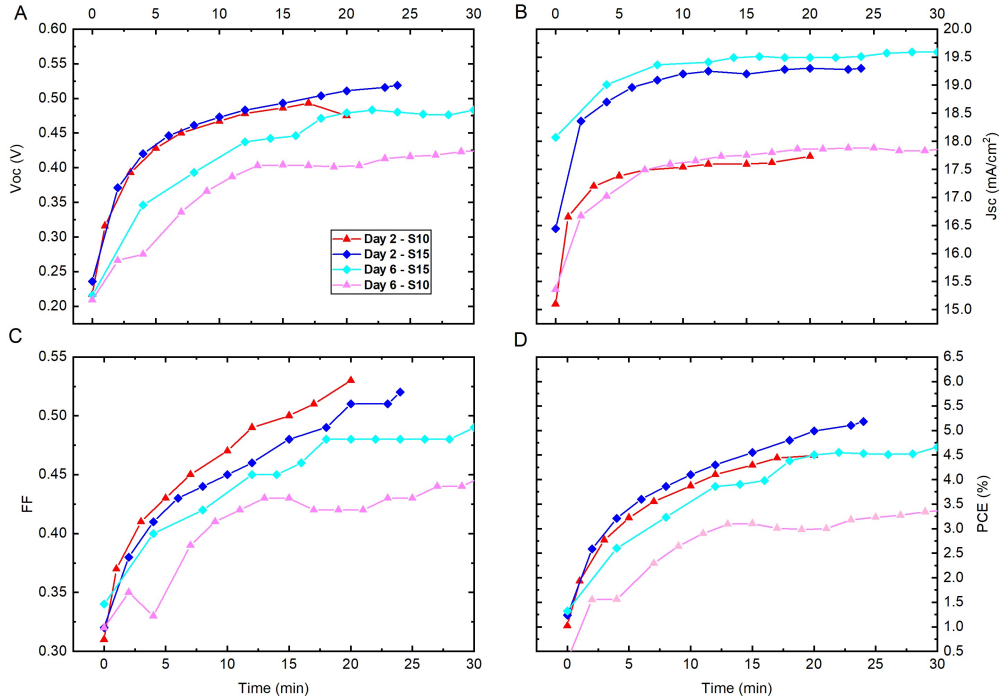
Figure 5.4: **Light soaking measurements**. *(A)VOC, (B) JSC, (C) FF and (D) PCE of two devices with different n-layer thickness after 2 and 6 days stored in an N_2 atmosphere.*

With the help of the absorption spectrum, the quantum confinement effect in quantum dots can be observed in the form of peaks. The broadening of the peak also indicates the size of the used quantum dots, which should be 2.88 nm for these specific QDs (*24*) (*36*).

The PbS-MPA ink absorbance was measured in order to compare and determine the absorbance peak. From Figure 5.5 (A), it can be observed a first excitonic peak at 935 nm, which approximately indicates the light wavelength at which this specific ink absorbs in the IR spectrum. With this information, the material's band gap is calculated to be ~ 1.33 eV, only 0.07 eV away from the ideal band gap for a single-junction solar cell (*37*). The absorbance curve of the p-type ink is also compared to the PbS-OA in solution curve. The peak of the latter is discerned at around 916 nm. Therefore, it can be stated that a minimal shift of the excitonic peak happens after the ligand exchange procedure, showing the little influence over the quantum confinement effect that the nanoparticles experience. Using the formula from Moreels et al. (*38*), the size of the QDs can also be calculated (see Appendix A.3). This leads to a size of 3.03 nm, which is in the range of accordance with previous experimental measurements.
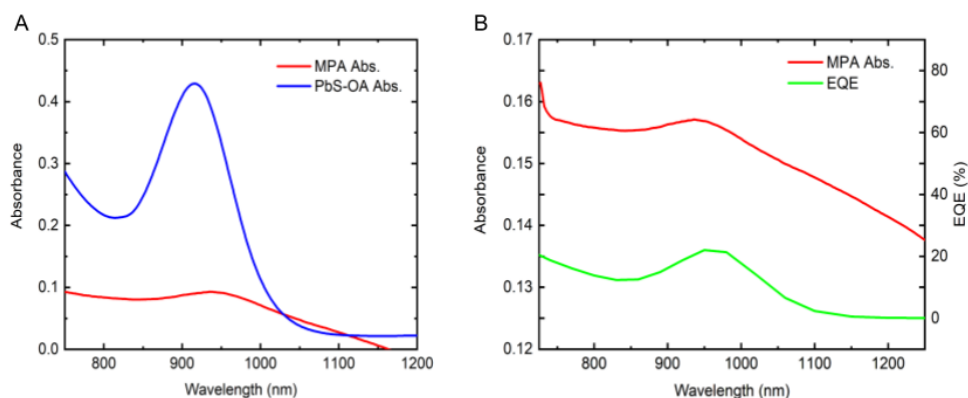
Figure 5.5: **Absorbance and EQE**. *Optical density spectrum of the MPA-PbS ink and EQE spectra of one of the ZnO-IPA fabricated devices.*

The EQE of one of the fabricated samples in ZnO-IPA was measured. A first excitonic peak at approximately 950 nm was obtained. It can be observed that the absorbance and the EQE peaks resemble, although they are not completely equal. The redistribution of light absorption caused by cavity effects (*31*) could have determined the differences between the absorption and the EQE spectra, establishing interference effects for specific wavelengths. It can also be concluded that the aggregation of the quantum dots during the fabrication process has nominal effects since the difference between peaks is only 10 nm approximately (*39*). Furthermore, even though the ink's stability is relatively poor, the device, after mounting, can be stable in air for several days.

5.2. New molecules

The biggest hurdle this type of solar cell encounters is its fabrication in air. Due to the water-based solvent used for the p-type layer, the deposition cannot be done inside the glovebox. This leads to additional stability issues. Therefore, SeMet and L-cysteine were tried for the substitution of the organosulfur molecule MPA. Both compounds are very similar to MPA, one containing an extra Se and amino group without the thiol and the other having an extra amino group, respectively.

SeMet was used as a first option, and different solvents were attempted to dissolve the powder in order for it to be an alternative for the p-type ligand exchange. DMF, dimethyl sulfoxide (DMSO), methanol, acetone and acetonitrile were observed to be ineffective. Nevertheless, it was detected that SeMet was miscible in BA. The finding was not highly positive, as BA is not an ideal solvent to proceed with the ligand exchange. Due to its molecular nature, the H-N bond is more easily replaceable

than C-Se leading to a complex tracking of the ligand exchange success (*40*).

L-cysteine was then chosen to replace the previously used molecule. This amino acid was not miscible in DMF either, but it showed some miscibility properties when mixed with DMSO. Therefore, to enhance the amalgamate, the solution was sonicated twice. Afterwards, the ligand exchange procedure took place. A very turbid solution was observed with no clear transparent layer to remove. For that reason, the centrifuge tube containing the mix was stirred for some time to help with the ligand exchange. Eventually, a thin translucent layer appeared and was removed in order to subsequently wash the solution once. During this process, it was already noticed that the colour of the cysteine-DMSO mixture indicated an inefficient reaction. Nevertheless, the sample was centrifuged so the pellet could be obtained and the supernatant removed. At first sight, the pellet was perceived to be very packed. It was later confirmed that the tested ligand did not work as the pellet could not be dissolved in BA, DMF, or DMSO, only in water. Ultimately L-cysteine was mixed with acetic acid, as it was supposed to be miscible according to the literature (*41*). Nonetheless, this trial was unsuccessful due to its insolubility.

Figure 5.6: **L-cysteine ligand exchange**. *Ligand solution.*

Hence, not SeMet nor L-cysteine were capable of solving the water-based p-type ink problem. The poor solubility encountered in the executed tests could be due to the lack of counterions of the materials. In L-cysteine, this could be avoided if chemical synthesis of L-cysteine with hydrochloric acid (HCl) were performed. The synthesis could be expected to be complete with good coverage, as reported in previous research (*42*).

6. Conclusion and Prospects

In conclusion, the newly constructed champion device can be said to overcome the reference VOC and JSC, as well as the PCE. Statistically, the champion device could not be reproduced repeatedly as the intended batch presented a noticeable thinner thickness in the n-type layer, which was determinant to the JSC and, consequently, to all the other figures of merit. Nevertheless, the passivation technique, along with the ZnO layer in IPA, presents promising results and appears as an interesting approach to optimize this type of solar cell. Furthermore, it could be observed that the ligand exchange procedure did not highly affect the quantum confinement effect after the process was completed. The device also presented a optimistic stability during the several days in which it was mounted, even though the inks' stability was poor. Overall, it has been proven that it is possible to fabricate a complete solution-processable solar cell with industrial-reproducible techniques. As for further research, it would be interesting to investigate the feasibility of a reverse p-i-n structure to avoid oxygen reactions and subsequent depositions in air that affect the stability of the device.

Concerning the alternative materials that were proposed in this research to substitute the MPA ligand, no satisfactory results were obtained. The water dependency of the molecules could not be discarded. However, it is positive to understand the miscibility properties of both chemicals to provide further information for future research and prevent vain attempts. L-cysteine synthesised in hydrochloric acid could be a possible option if its solubility is proved to be higher. Regardless, the performance of the two materials using water as solvent could be tested to measure and evaluate their characteristics in a mounted device.

References

1. R. A. M. Lameirinhas, J. P. N. Torres, J. P. de Melo Cunha, *Energies* vol. 15 (2022).

2. G. Conibeer, *Materials Today* **10**, 42–50 (2007).

3. A. P. Litvin *et al.*, *Journal of Materials Chemistry A* **5**, 13252–13275 (2017).

4. W. Chi, S. K. Banerjee, *Chemical Engineering Journal* **426**, 131588 (2021).

5. T. Sogabe, Q. Shen, K. Yamaguchi, *Journal of Photonics for Energy* **6** (2016).

6. P. Atkins, J. D. Paula, *Atkins' Physical Chemistry, 11th Ed.*

7. C. Honsberg, S. Bowden, *Photovoltaics Education Website.*

8. D. Peroulis *et al.*, *Conduction Mechanisms in Organic Semiconductors* (Springer Netherlands, 2012), pp. 493–500.

9. C. Frank-Rotsch, N. Dropka, P. Rotsch, *III Arsenide* (Elsevier, 2019), pp. 181–240.

10. M. I. Dyakonov, *Basics of Semiconductor and Spin Physics*, vol. 157.

11. J. Morrison, *Modern Physics for Scientists and Engineers.*

12. J. Nelson, *The Physics of Solar Cells* (Imperial College Press, 2003).

13. A. Kahn, *Materials Horizons* **3**, 7–10 (2016).

14. T. Dittrich, *Materials Concepts for Solar Cells.*

15. C. Poole, I. Darwazeh, *Microwave semiconductor materials and diodes* (Elsevier, 2016), pp. 355–393.

16. A. Shah, Ed., *Solar Cells and Modules* (Springer International Publishing, 2020), vol. 301.

17. A. A. Ojo, W. M. Cranton, I. M. Dharmadasa, *Next Generation Multilayer Graded Bandgap Solar Cells* (Springer International Publishing, 2019).

18. J. Liu, K. Xian, L. Ye, Z. Zhou, *Advanced Materials* **33**, 2008115 (2021).

19. M. J. Speirs, PhD thesis, University of Groningen, 2017.

20. P. Wang *et al.*, *Advanced Functional Materials* **29**, 1807661 (2019).

21. P. Guyot-Sionnest, *Comptes Rendus Physique* **9**, 777–787 (2008).

22. S. Kilina, S. Ivanov, S. Tretiak, *Journal of the American Chemical Society* **131**, 7717–7726 (2009).

References

23. H. Zhao, F. Rosei, *Chem* **3**, 229–258 (2017).

24. D. Bederak, PhD thesis, University of Groningen, 2021.

25. M. Ulfa, *AIP Conference Proceedings* **1586**, 191–197 (2014).

26. D. M. Balázs, PhD thesis, University of Groningen, 2018.

27. Y. Cheng, E. S. Arinze, N. Palmquist, S. M. Thon, *Nanophotonics* **5**, 31–54 (2016).

28. L. M. Nikolenko, V. F. Razumov, *Russian Chemical Reviews* **82**, 429–448 (2013).

29. J. Chen *et al.*, *ACS Energy Letters* **6**, 1970–1979 (2021).

30. M. Yuan *et al.*, *Small* **18**, 2102340 (2022).

31. V. M. Goossens, N. V. Sukharevska, D. N. Dirin, M. V. Kovalenko, M. A. Loi, *Cell Reports Physical Science* **2**, 100655 (2021).

32. J. R. Vig, *Handbook of Semiconductor Wafer Cleaning Technology*, ISSN: 00396028 (1993).

33. S.-C. Liu *et al.*, *Journal of the American Chemical Society* **141**, 18075–18082 (2019).

34. C. Kim *et al.*, *ACS Applied Materials and Interfaces* **12** (2020).

35. S. Shao *et al.*, *Energy Environmental Science* **9**, 2444–2452 (2016).

36. B. D. Geyter, Z. Hens, *Applied Physics Letters* **97**, 161908 (2010).

37. S. Kahmann, M. A. Loi, *Journal of Materials Chemistry C* **7**, 2471–2486 (2019).

38. I. Moreels *et al.*, *ACS Nano* **3**, 3023–3030 (2009).

39. H. Aqoma, S.-Y. Jang, *Energy Environmental Science* **11**, 1603–1609 (2018).

40. J. A. Dean, *Materials and Manufacturing Processes* **5**, ISSN: 15322475 (1990).

41. O. MJ., *The Merck Index - An Encyclopedia of Chemicals, Drugs and Biologicals. Cambridge, UK: Royal Society of Chemistry.*

42. R. Lu, *Huagong Shikan* **24**, 17–20 (2010).

A. Appendix

A.1. Experimental quantities

The PbS-MPA ink was prepared for each batch using the values noted in Tables A.1 and A.2.

Batch	PbS-OA	Hexane	MPA	DMF	BA
15x15	0.05048	1.9495	0.3	1.7	0.2
30x30	0.154849	1.845150	0.006675	1.993325	0.2

Table A.1: Volumes in mL used to prepare the p-type ink.

Batch	PbS-OA in hexane	MPA in DMF	Ink concentration (conc).
15x15	8	0.0383	40
30x30	8	0.0383	40

Table A.2: Concentrations in mg/mL used to prepare the p-type ink.

The PbS-PX$_2$ ink was prepared for each batch using the values noted in Tables A.3, A.4 and A.5.

Batch	PbS-OA	Hexane	BA
15x15	0.236635	7.263365	0.441176
30x30	0.677468	6.322531	0.411765

Table A.3: Volumes in mL used to prepare the n-type ink.

Batch	PbI$_2$	PbBr$_2$	AA
15x15	0.553212	0.088082	0.055498
30x30	0.516331	0.164420	0.051798

Table A.4: Weights in g used to prepare the n-type ink.

Batch	PbS-OA in hexane	PbI$_2$	PbBr$_2$	AA	Ink conc.
15x15	10	0.1	0.04	0.06	170
30x30	10	0.1	0.04	0.06	170

Table A.5: Concentrations in mg/mL used to prepare the n-type ink.

A.2. Wavelength to photon energy

The following formula has been used in order to convert the absorption exciton peaks into eV:

$$E = \frac{1239.8}{\lambda} \tag{A.1}$$

where λ is the wavelegth in nm.

A.3. Quantum dot size

The size of the QD can be calculated using the following:

$$E_0 = 0.41 + \frac{1}{0.0252d^2 + 0.283d} \tag{A.2}$$

where E_0 represents the bandgap in eV and d the QD's size in nm.